Visualization and Analysis of Deep Water Asteroid Impacts

Raphael Imahorn*   Irene Baeza Rojo†   Tobias Günther‡

Computer Graphics Laboratory, ETH Zürich

ABSTRACT

As evident by the Earth's history, severe asteroid impacts pose a significant threat to all species living on our planet. The severity of an impact is difficult to predict due to the vast amount of dependent parameters and thus the potential consequences on climate, plate tectonics and organisms are not yet fully understood. To improve our understanding of the threats imposed by asteroid impacts, scientists at Los Alamos National Laboratory conducted an ensemble simulation for varying impact scenarios into deep water oceans. The IEEE Scientific Visualization Contest 2018 is dedicated to the visual analysis of these asteroid impact simulations. In this paper, we apply a number of recent state-of-the-art visualization techniques to visually compare and analyze the varying impact scenarios. We discuss both automatic approaches applicable to an in-situ analysis, as well as interactive approaches for a detailed exploration.

1 INTRODUCTION

A severe asteroid impact such as by the Chicxulub asteroid 65.5 million years ago can drastically change the climate, destroy ecosystems, alter plate tectonics and cause mass extinctions [7]. For this reason, NASA currently tracks a number of potentially hazardous asteroids, automatically scans for potential impacts using their Sentry system, and is keenly interested in the potential risk assessment of an impact on Earth. Since any mission to deflect an asteroid will be a major effort, it is important to understand how hazardous an impact scenario can be. Thus, scientists from Los Alamos National Laboratory conducted a numerical multi-physics hydrodynamics simulation using the xRage code [2] to gain new insights into possible impact scenarios. Since about 71% of the Earth's surface is covered by water, the simulations concentrate on asteroid impacts in deep water oceans, which might lead to tsunamis. The IEEE Scientific Visualization Contest 2018 encourages visualization researchers to visually analyze the provided ensemble simulations that explore varying asteroid sizes, impact angles and airbursts.

In our submission, we apply a wide range of state-of-the-art visualization techniques to analyze the asteroid decay before impact, the generated waves for various ensemble members, the pressure waves, the material distribution, the attribute correlations and passageways of water vapor into the stratosphere. First, overviews are generated automatically, which could be integrated in an in-situ manner into the simulation pipeline. We utilize a diverse set of tools, including Monte Carlo based integrators for Lagrangian transport analysis, linear optimization for interactive visibility adjustment of pathlines and streaklines, derived Eulerian fields to study the vector fields, coordinated views with two-dimensional histograms for interactive linking and brushing, and immersive technologies such as virtual and augmented reality. Our visualizations provide a comprehensive view on the influences of the individual ensemble parameters, which gives better means to assess the associated risk factors.

---

*e-mail:imahornr@student.ethz.ch

†e-mail:irene.baeza@inf.ethz.ch

‡e-mail:tobias.guenther@inf.ethz.ch

2 CONTEST DATA

First, we briefly summarize the provided contest data. An overview of the ensemble members and their associated naming convention are shown in Table 1. The four basic scalar attributes include volume fraction of water (V02), volume fraction of asteroid (V03), temperature (TEV in eV) and pressure (PRS in μbar). Some ensemble members additionally contain density (RHO in $\frac{g}{cm^3}$), velocity (XDT, YDT, ZDT in $\frac{cm}{sec}$), sound speed (SND in $\frac{cm}{sec}$), material ID (MAT) and the grid refinement level (GRD). The three ensemble parameters are the airburst (none, 5 km or 10 km), the asteroid diameter (100 m or 250 m) and the impact angle (45° or 60°). An airburst can occur if the asteroid interacts with the atmosphere and therefore explodes before impacting the surface. We used the rectilinear grids provided for the contest and focused on the 300^3 and the $460 \times 280 \times 240$ resolutions, due to the similar number of grid points.

Preprocessing. The first step in most visualization pipelines is the preprocessing of the data to remove inconsistencies, errors and missing values. Only in the four-attribute series of YA11, density (RHO) appeared as fifth attribute in 36 time steps, which we neglected for consistency. Let i be the time step index. Missing cycle indices c_i were taken from the file name. When the simulated time t_i was missing, we computed an estimated time $\hat{t}_i$ as follows. If there existed a later time step n with valid cycle index c_n and simulated time t_n, we linearly interpolated between the already processed time of the previous step $\hat{t}_{i-1}$ and the next valid time t_n. Otherwise, we extrapolated from the previous time step by considering the time difference d_i between two cycles. This leads to the formula:

$$\hat{t}_i = \begin{cases} (1-f) \cdot \hat{t}_{i-1} + f \cdot t_n, & f = \frac{c_i - c_{i-1}}{c_n - c_{i-1}} \quad \exists n \\ \hat{t}_{i-1} + (c_i - c_{i-1}) \cdot d_i & else \end{cases} \quad (1)$$

Some files of the YC31 sequence had wrong spatial meta data, i.e., the grid resolution and the position of the origin were incorrect. We fixed this by always using the spatial information of the first time step in the ensemble. Missing attributes were linearly interpolated between the last (preprocessed) time step and the next valid time step. When there were no previous or later valid time step available, the time step was removed. Similarly, this interpolation was used for points where the *vtkValidPointMask* stated an invalid point. An example of invalid values that were replaced by linearly interpolating between valid adjacent time steps is shown in Fig 1. To reduce the loading time, all files were stored in the VTK compressed format.

Data	Grid	Airburst	Size	Angle	Attr.
yA11	300^3	–	100 m	45°	four
yB11	300^3	5 km	100 m	45°	four
yC11	300^3	10 km	100 m	45°	four
yA31	300^3, 500^3	–	250 m	45°	all
yB31	$460 \times 280 \times 240$	5 km	250 m	45°	all
yC31	$460 \times 280 \times 240$	10 km	250 m	45°	all
yA32	300^3	–	250 m	60°	four

Table 1: Overview of the used data with grid resolution, airburst height (if any), asteroid diameter, impact angle and the available attributes (only four or all).

3 VISUALIZATIONS

Scientific visualization is a key component to solving modern large-scale data science problems. To utilize its full potential, it must be carefully tailored to the application. In our paper, we discuss multiple opportunities that visualization provides to gain new scientific insight in the context of asteroid simulations, namely by overview generation, interactive exploration, comparison and presentation.

3.1 General Overview

Since the ensemble data is very large, we believe that the most practical approach to a very general overview leads through an automatic generation of animated visualizations. Most importantly, these visualizations could be generated in-situ at the highest available data resolution and for every future simulation run, allowing domain scientists a much faster view into their data. To obtain an overview, we first render animations of direct volume renderings for each attribute of the ensemble members, as shown for selected attributes in Fig. 2. For ensemble members with velocity data, we also generate animations of derived differential scalar properties, namely divergence and vorticity, which provide further information on the flow behavior. We render each animation from three view points: from the side (asteroid moves left to right), from the front (asteroid approaches camera) and from the opposite side (asteroid moves right to left) where we clip half the volume away to look into the domain. This leads us to the following first observations.

3.2 Asteroid Size

When the asteroid diameter is only 100 m and the impact angle is 45° (Y[ABC]11 series), the asteroid never impacts the water. Fig. 3a shows for each scenario three different time steps of the asteroid approaching the water. For YB11 and YC11, the airburst causes the asteroid to decompose before reaching the water. However, even without airburst in YA11 the asteroid does not reach the water surface. Based on this observation, we conclude that this impact configuration does not pose a threat of tsunamis.

When the asteroid diameter is 250 m and the impact angle is 45° (Y[ABC]31 series), the asteroid impacts the water in every airburst configuration. Fig. 3b shows the water fraction (V02) for the three configurations, where we observe that without an airburst (YA31) the asteroid has a stronger impact, while the existence of an airburst dampens the impact the higher the airburst altitude. In order to study the effect and the height of the waves created by the impact further, we use other attributes, explained later in Section 3.5, since the water volume of the splashes occludes the crater and makes the observation of the wave formations difficult.

3.3 Impact Angle

In Fig. 4, we study the influence of the impact angle in more detail. In particular, we concentrate on two phenomena: the shape of the pressure shock wave and the passageway of water vapor into the stratosphere. In the top row, we see that the pressure (PRS) wave of the 45° impact has a more uniform pressure distribution and a rounder shape compared to the 60° impact. We assume that the pressure distribution along the wave influences how far the wave travels and how strong its impact on shorelines is. The bottom row displays the water (V02). We see significant differences in the ways how water vapor is lofted into the stratosphere. On the 60° impact, a large amount of water travels with high speed along the entry corridor of the asteroid, causing a swift uplift of water above the tropopause. Water vapor is among the strongest greenhouse gases [9] and is thus expected to have a notable influence on the climate, since material lofted into the stratosphere can remain there for a long time.

3.4 Pre-Impact Asteroid

In Fig. 5, we have a closer look at the entry and decay of the asteroid in the YA11 series. The air friction causes the asteroid to decay, leaving a tail of material in the atmosphere. As the asteroid descends, the head quickly decelerates, while the tail material follows in its wake. As more tail material catches up, the head is split and driven apart. The strong shear along the entry corridor creates two vortices that trap the asteroid material of the head. Most of the asteroid tail passes between the two vortices and enters a standing vortex bubble. Eventually, the vortex bubble and the two vortices break down, while most material slowly ascends in the wake of the asteroid, presumably due to a pressure gradient. Similar observations can be made for YB11 and YC11, but at higher altitude due to the airbursts.

3.5 Wave Height

In this section, we study the creation of waves for the different airburst scenarios in more detail by comparing the wave propagation as well as the maximum wave height in the Y[ABC]31 series. Due to the radial symmetry of the wave, we concentrate on the central XY-slice. To compute the wave height $h(x)$, we determine for each x-coordinate the height of the largest vertical density (RHO) partial:

$$h(x) = \arg\max_{y} \left| \frac{\partial \rho(x,y)}{\partial y} \right| \qquad (2)$$

Fig. 6 shows three time step after the impact where the difference in crater size becomes apparent. The deepest crater and highest waves are created by the asteroid with no airburst (YA31). The propagation of the created wave is proportional to its height, as higher waves will propagate horizontally further than smaller ones.

3.6 Flow Visualizations

Derived Properties. Fig. 2g demonstrates the direct volume renderings of divergence and vorticity in the YA31 series. The top row shows a high divergence at the impact site, which is due to the explosion-like expansion that pushes a shock wave outward. In consequence, a strong air compression is apparent at the front of the shock wave, since the air mass is too viscous to give way. In Fig. 2h, vorticity indicates strong vortical motion in the air above the impact site. As apparent in the video, multiple smaller vortices are created in the rising water vapor plume, which is also evident in the V02 attribute. In addition, the strong shear layer in the wake of the asteroid creates a vortex below the entry corridor. The vorticity in the wake of the asteroid is not due to vortical motion, but rather an artifact of strong shear that vorticity also responds to.

Monte Carlo FTLE. The finite-time Lyapunov exponent [8], commonly used in time-dependent fluid flows, is an approximate measure to locate hyperbolic Lagrangian coherent structures, which act as transport barriers that guide the advection. In order to correctly visualize FTLE ridges that can become arbitrarily sharp and very complex, recent work by Günther et al. [3] proposed an unbiased Monte Carlo-based rendering approach that treats the FTLE field as participating media with single-scattering. We use this technique in the Y[ABC]31 ensembles, shown in Fig. 7a, where we can observe how the airburst of the asteroid affects the width of the entry corridor formed by the falling asteroid, the uplift paths of particles rising up into the stratosphere and the high degree of turbulence that followed the impact. The ensemble member with no airburst (YA31) lifted the water higher up than the impacts with airburst, due to its stronger impact. Thus, in the YA31 series, we see vortical motion left of the impact site (probably formed by the forward rising water vapor plume) and below the entry corridor (probably formed due to the strong shear along the entry corridor).

3.7 Opacity Optimization

Next, we concentrate on the interactive visualization of flow data, for which we use the opacity optimization of Günther et al. [5]. Their method allows the user to define an importance measure for geometric primitives, which makes relevant objects visible among the context geometry by automatically adjusting the transparency.

Pathlines. First, we study the Y[ABC]31 series, which have vector field attributes. In each ensemble member, we traced $8,000$ particles over the whole simulation duration, which resulted in dense line sets. Directly plotting these line sets would produce a cluttered view, where we cannot discern interesting insights about the data, which is commonly know as the occlusion problem [4,5] in visualization. Fig. 7b shows the results obtained when using the opacity optimization method with the asteroid fraction as importance measure. Trajectories with high asteroid fraction (red) are mainly focused in the impact area, while the remaining particles with lower asteroid fraction (blue) give the visualization a general context and help to better distinguish from where the main trajectories are coming and where the water and asteroid particles travel right after impact. Without an airburst, asteroid particles travel compactly on their falling path (left), while the presence of an airburst increases the spread of asteroid particles in the entry corridor and distributes more particles upwards after the impact.

Streaklines. While pathlines display the position of particles for all time steps in one image, streaklines are much better suited to convey spatially coherent structures. Figuratively speaking, we can imagine streaklines as the trails of smoke or ink being constantly injected at a seeding point. Since all particles of a streakline exist in the same time slice, these integral curves do not self-intersect. Using the YA31 data set, we created a set of $5.9k$ streaklines by injecting particles from randomly distributed seed points. In Fig. 7c, we use both water fraction (V02) and curvature as importance measures to highlight water particle paths and vortical structures. As expected, the biggest water particle concentration occurs at the impact site, allowing us to see the forward-rotating motion of the rising water vapor plume. The entry corridor itself induces a pressure gradient that draws in particles after the impact. The uplift and the movement in the corridor are both made visible by the streaklines.

3.8 Linking and Brushing

An automatic generation of visualizations as in Section 3.1 can never replace an interactive and user-centered data exploration. In the following, we concentrate on more advanced interactive exploration techniques. A common visualization task on multi-variate data is to look for correlations among the attributes. For this reason, we compute scatterplot matrices, showing a scatterplot for each pair of attributes in Fig. 8a. The evolution of the patterns can be animated over time. The user can select a single scatterplot for closer inspection and may use an interactive brush to filter selected regions. In Figs. 8b to 8d, for instance, we select a combination of sound speed (SND) and temperature (TEV) to filter the water fraction (V02), showing only the waves or only the water vapor in the atmosphere.

Further, we analyze the evolution of water fraction (V02), asteroid fraction (V03) and air over time in Fig. 9 by creating a scatterplot in barycentric coordinates. In this plot, we see how the distribution of the three materials changes over time, starting with a clear separation, mixing upon impact and the vanishing of asteroid material over time.

3.9 Virtual and Augmented Reality

Immersive display technologies provide new means to step into a three-dimensional world, enabling better depth perception and new forms of interactive data exploration. To explore the capabilities of virtual reality (VR) and augmented reality (AR) devices for visualization, we developed two demos, which show the asteroid impact sequence YA31 using direct volume rendering of the water fraction (V02 in blue) and the asteroid fraction (V03 in orange). For the VR demo we use an Oculus Rift, and for AR we use a Microsoft HoloLens. Both demos were implemented in native C++ with Direct3D, using the native APIs. Fig. 10 (left) shows two frames of a VR screen capture, where the user explores the domain and interacts with clipping planes to see the interior of the water vapor plume, the asteroid material, the wave creation and the deformation of the

crater. In Fig. 10 (right), the AR scene is shown from the eyes of the user, embedding the impact sequence in the real world. While VR has a larger field of view and better visual contrast, AR has more potential for collaborative exploration and education.

4 IMPLEMENTATION

We used the Visualization Tool Kit (VTK) [10] to implement our interactive exploration tool. Aside from the interactive navigation, attribute selection and exploration with coordinated views, we used the tool to preprocess the data, render animations, trace pathlines, compute the wave heights and plot the histograms. For pathline tracing and the FTLE calculation, we used a fourth-order Runge-Kutta integrator. The color transfer functions are based on built-in transfer functions of ParaView [1] and on ColorBrewer [6].

5 CONCLUSION

In this work, we demonstrated a wide range of recent state-of-the-art scientific visualization techniques to explore, compare and present structures in the ensemble members of an asteroid impact simulation. We have shown how visualization can assist the data analysis in many ways, including in-situ capable automatic generation of overviews, high-quality visualizations of volume and flow data and various interactive exploration techniques comprising linking and brushing, Monte Carlo integration, linear optimizations and finally through immersive head-mounted display technologies. We hope that the visualizations give inspiration to the domain scientists and that some of the methods will be adapted into their workflows.

REFERENCES

[1] J. Ahrens, B. Geveci, C. Law, C. Hansen, and C. Johnson. Paraview: An end-user tool for large data visualization. *The visualization handbook*, 717, 2005.

[2] M. Gittings, R. Weaver, M. Clover, T. Betlach, N. Byrne, R. Coker, E. Dendy, R. Hueckstaedt, K. New, W. R. Oakes, D. Ranta, and R. Stefan. The RAGE radiation-hydrodynamic code. *Computational Science and Discovery*, 1(1):015005, 2008.

[3] T. Günther, A. Kuhn, and H. Theisel. MCFTLE: Monte Carlo rendering of finite-time Lyapunov exponent fields. *Computer Graphics Forum (Proc. EuroVis)*, 35(3):381–390, 2016.

[4] T. Günther, C. Rössl, and H. Theisel. Opacity optimization for 3D line fields. *ACM Transaction on Graphics (Proc. SIGGRAPH)*, 32(4):120:1–120:8, 2013.

[5] T. Günther, H. Theisel, and M. Gross. Decoupled opacity optimization for points, lines and surfaces. *Computer Graphics Forum (Proc. Eurographics)*, 36(2):153–162, 2017.

[6] M. Harrower and C. A. Brewer. Colorbrewer.org: An online tool for selecting colour schemes for maps. *The Cartographic Journal*, 40(1):27–37, 2003. doi: 10.1179/000870403235002042

[7] P. Schulte, L. Alegret, I. Arenillas, J. A. Arz, P. J. Barton, P. R. Bown, T. J. Bralower, G. L. Christeson, P. Claeys, C. S. Cockell, et al. The Chicxulub asteroid impact and mass extinction at the Cretaceous-Paleogene boundary. *Science*, 327(5970):1214–1218, 2010.

[8] S. C. Shadden, F. Lekien, and J. E. Marsden. Definition and properties of Lagrangian coherent structures from finite-time Lyapunov exponents in two-dimensional aperiodic flows. *Physica D: Nonlinear Phenomena*, 212(3-4):271–304, 2005. doi: 10.1016/j.physd.2005.10.007

[9] S. Solomon, K. H. Rosenlof, R. W. Portmann, J. S. Daniel, S. M. Davis, T. J. Sanford, and G.-K. Plattner. Contributions of stratospheric water vapor to decadal changes in the rate of global warming. *Science*, 327(5970):1219–1223, 2010.

[10] K. M. Will Schroeder and B. Lorensen. *The Visualization Toolkit*. Kitware, 4th ed., 2006.

(a) Material index (MAT) (b) Raw data (with missing values) (c) Preprocessed data
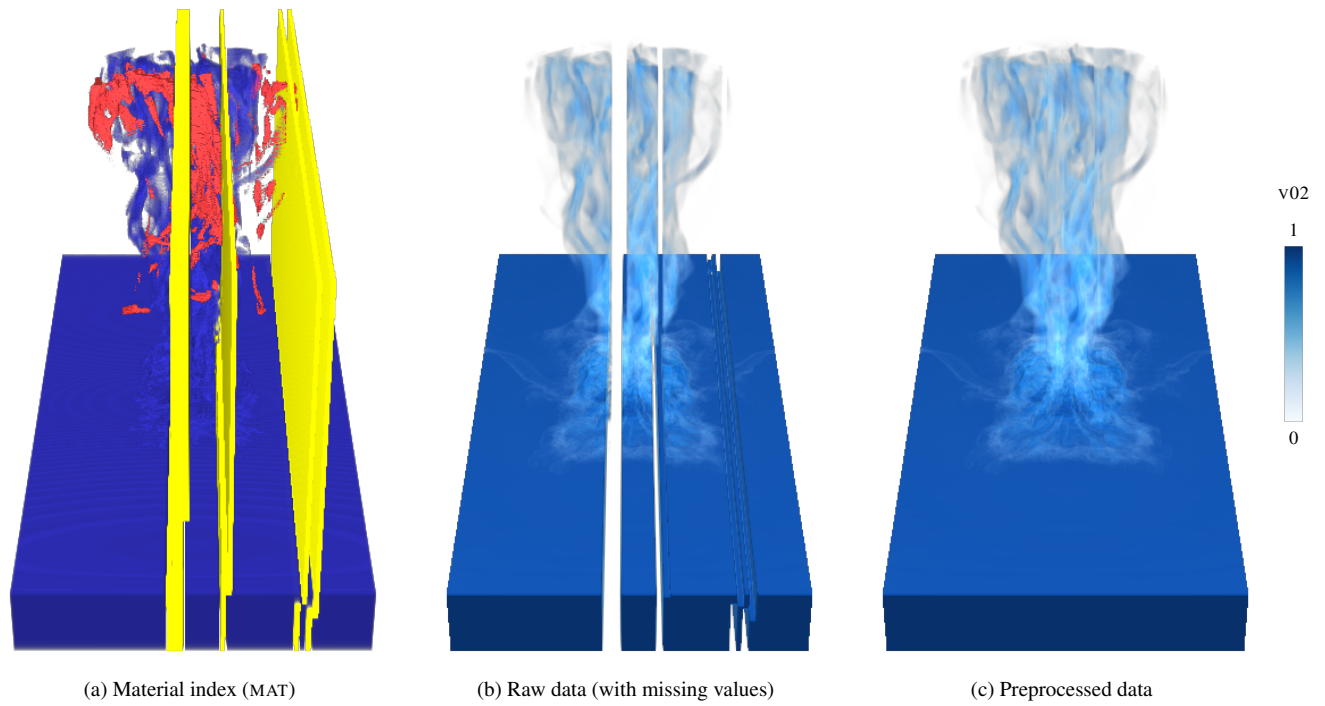
Figure 1: In order to remove inconsistencies and errors in the raw data, we preprocessed all ensemble members to fill missing values, here illustrated for a time step in the YC31 series. The left image shows the material indices: blue means mostly water, red mostly asteroid and yellow are invalid material indices. The middle image shows a volume rendering of the raw water fraction (V02), in which missing values are apparent. The right image show the result after our preprocessing step. Since the temporal distance between time steps is small, interpolation errors are barely noticeable.

(a) Pressure (PRS)　　　　　(b) Temperature (TEV)　　　　　(c) Water fraction (V02)

(d) Asteroid fraction (V03)　　　　　(e) Density (RHO)　　　　　(f) Sound speed (SND)

side view　　　　　front view　　　　　opposite side (with clipping plane)

(g) Divergence

side view　　　　　front view　　　　　opposite side (with clipping plane)

(h) Vorticity
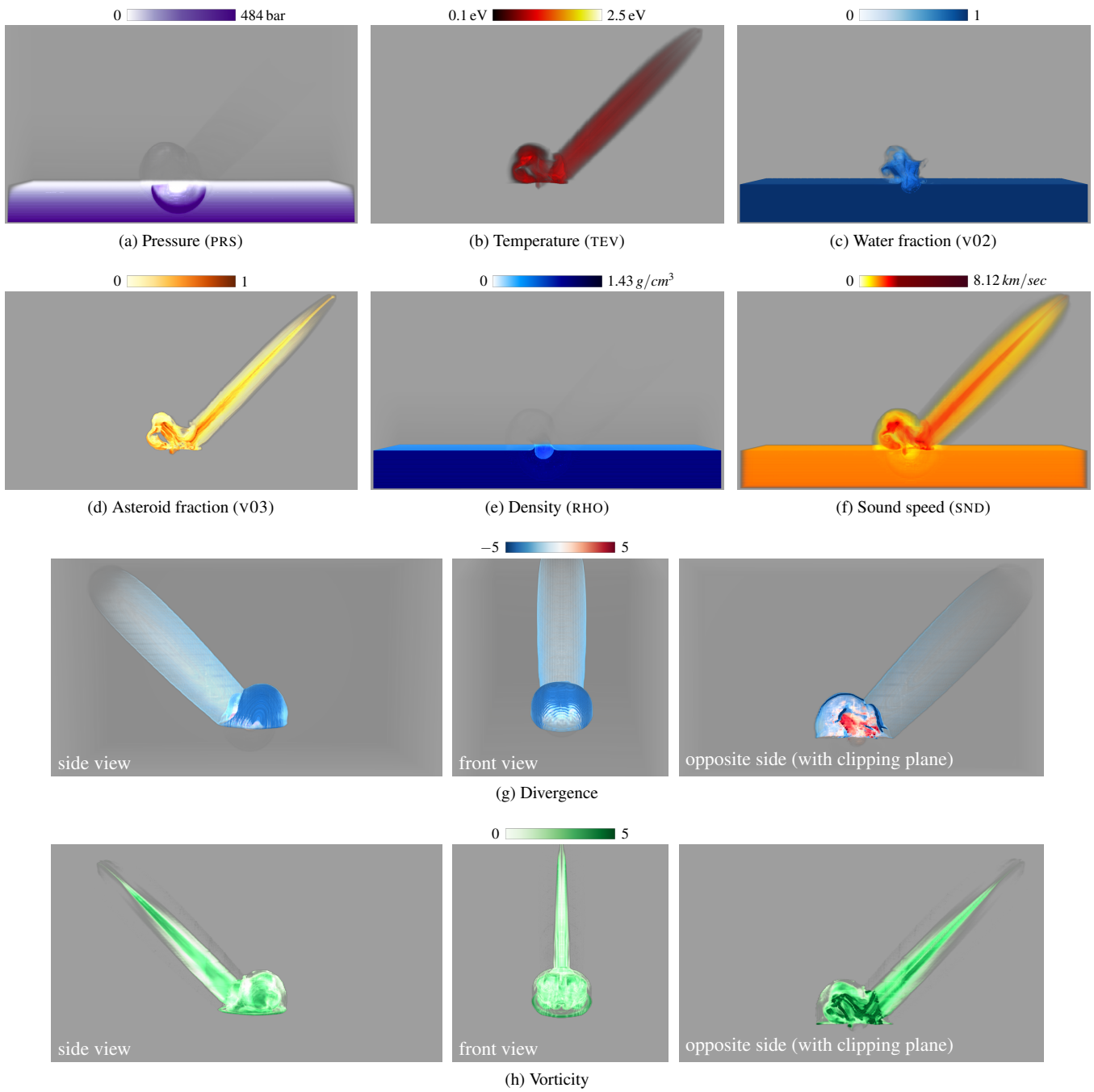
Figure 2: To familiarize with the data, we first automatically generate visualizations of all attributes for all ensemble members from three different view points. For the third view point, a cutting plane is placed to look into the domain. Selected visualizations are shown above for the YA31 series (diameter 250 m, impact angle of 45° and no airburst), showing the attributes shortly after impact. When velocity fields are available, we also generate visualizations of derived scalar fields such as divergence and vorticity, as shown in Figs. 2g and 2h, which identify areas of compression and expansion, as well as high turbulence.
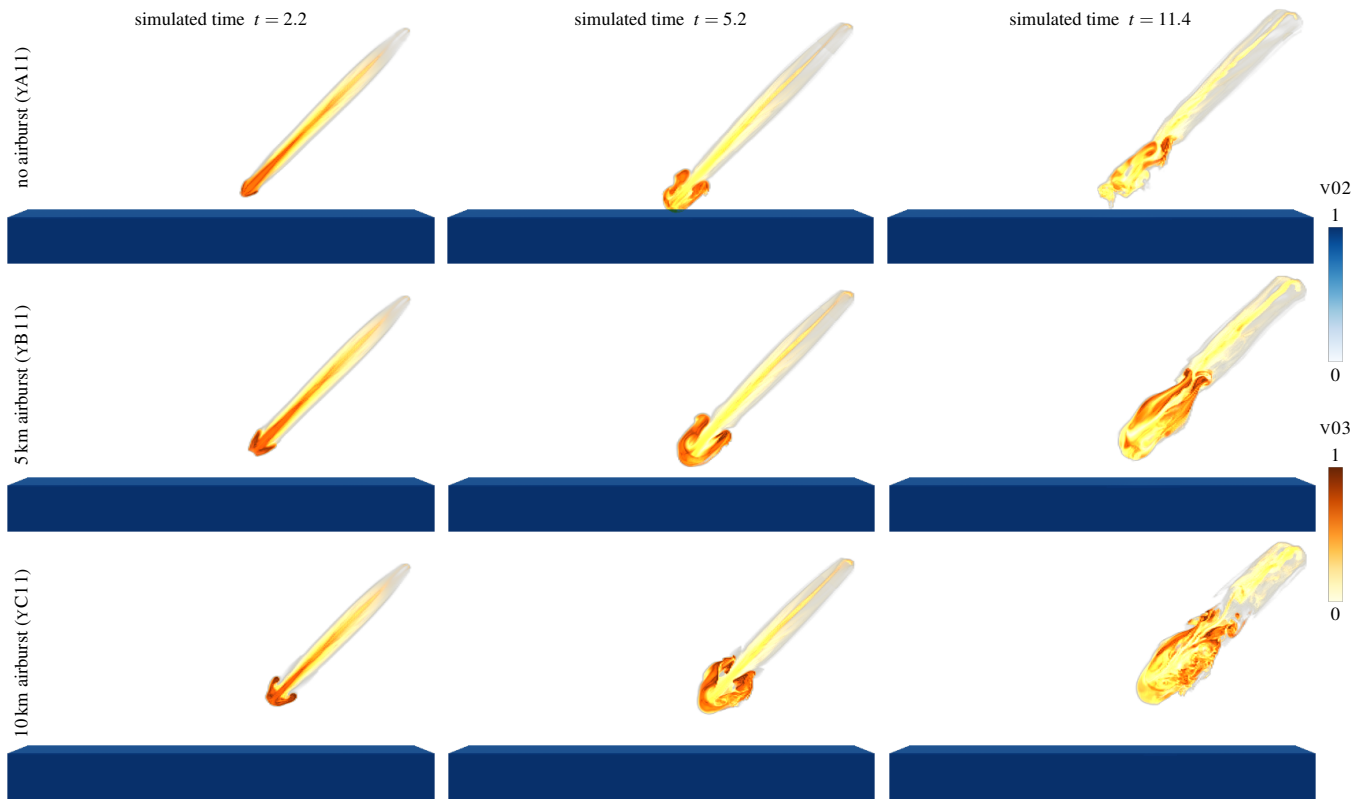
(a) Comparison of different airburst heights for the small asteroids (100 m size): no airburst (top), 5 km (middle) and 10 km (bottom). The volume renderings show the water fraction (V02) and the asteroid fraction (V03). In the columns, different time steps are shown, displaying the entry and decay of the asteroids. It becomes apparent that none of the 100 m asteroids impacts in the water, independent of the airburst height.
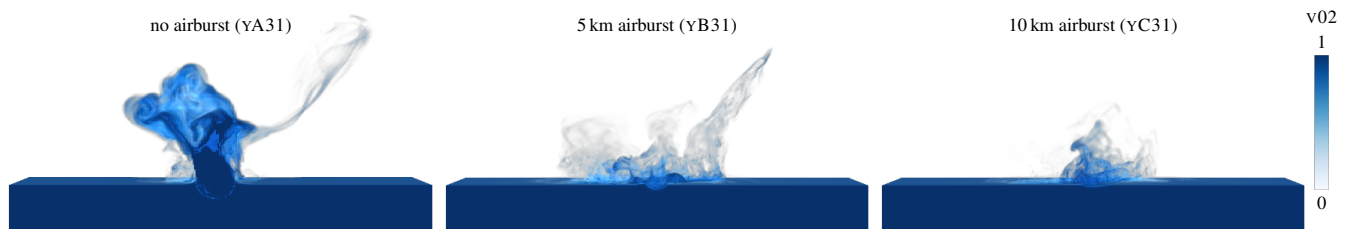
(b) The above volume renderings show the water fraction (V02) after 15 sec of the simulation for the different airburst scenario. Here, the large asteroids were chosen (250 m) with an impact angle of 45°, which resulted in a water impact for all cases. Without airburst (left), more kinetic energy is transferred into the water, creating a larger splash than in the two scenarios with airburst (middle and right).

Figure 3: Comparison of the ensemble members regarding the influence of asteroid size and airbursts on the impact and water vapor plume.
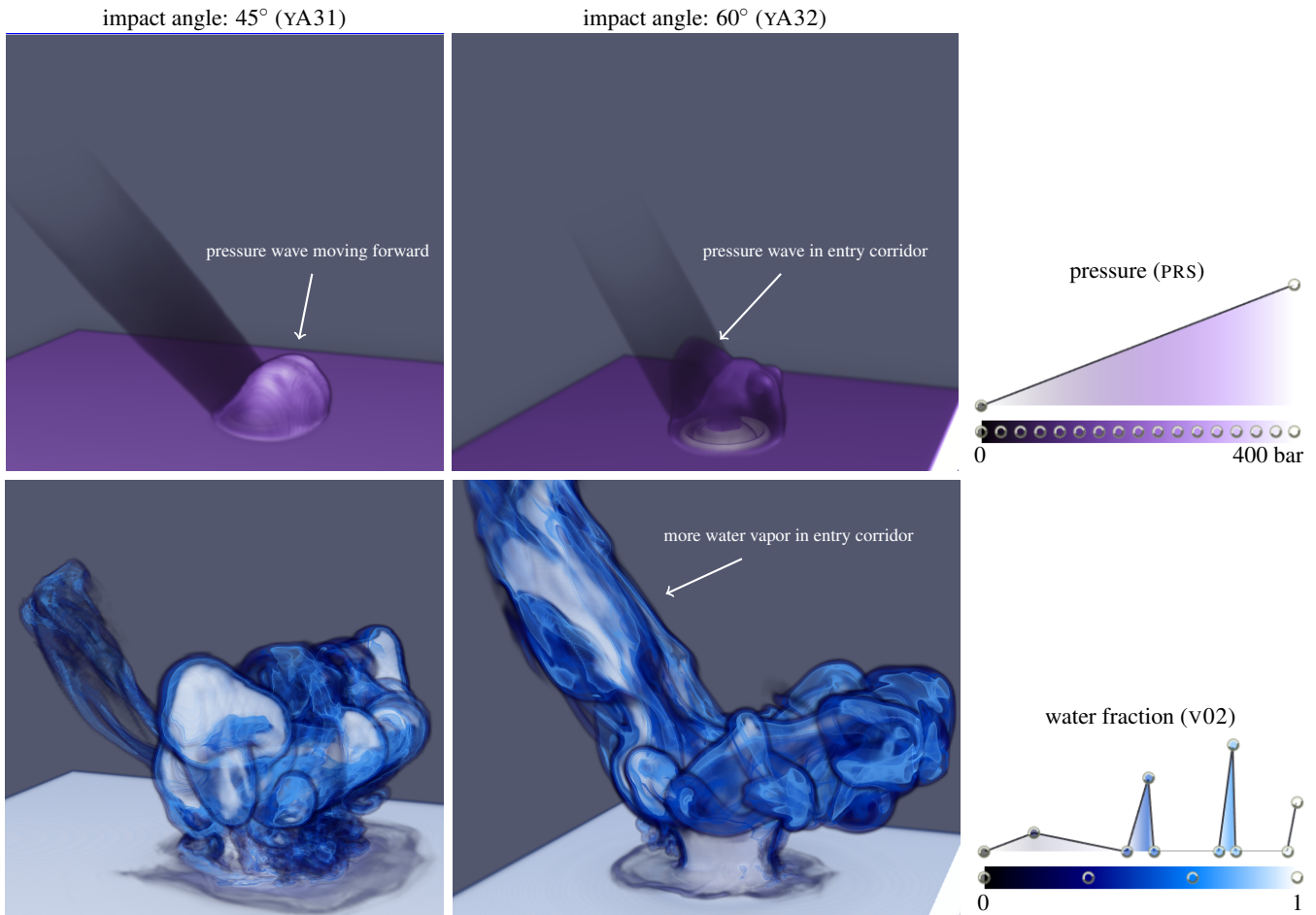
Figure 4: Comparison of different impact angles, showing differences in the pressure wave (top) and the passageway of water into the atmosphere (bottom) for an asteroid diameter of $250\,m$ and no airburst. The images were rendered with Nvidia IndeX. Top: The pressure wave of the $45°$ angle has a higher magnitude and a more uniform shape. During the $60°$ angle impact, bumps form on the pressure wave, including a pressure wave traveling upwards in the asteroid entry corridor. Bottom: The water vapor plume of the $60°$ impact moves higher upwards along the asteroid entry corridor, which was indicated above by the pressure wave, lifting more material upwards into the stratosphere. We conclude that a steeper impact angle might cause a stronger influence on the climate due to more greenhouse gas (water vapor) entering the stratosphere.
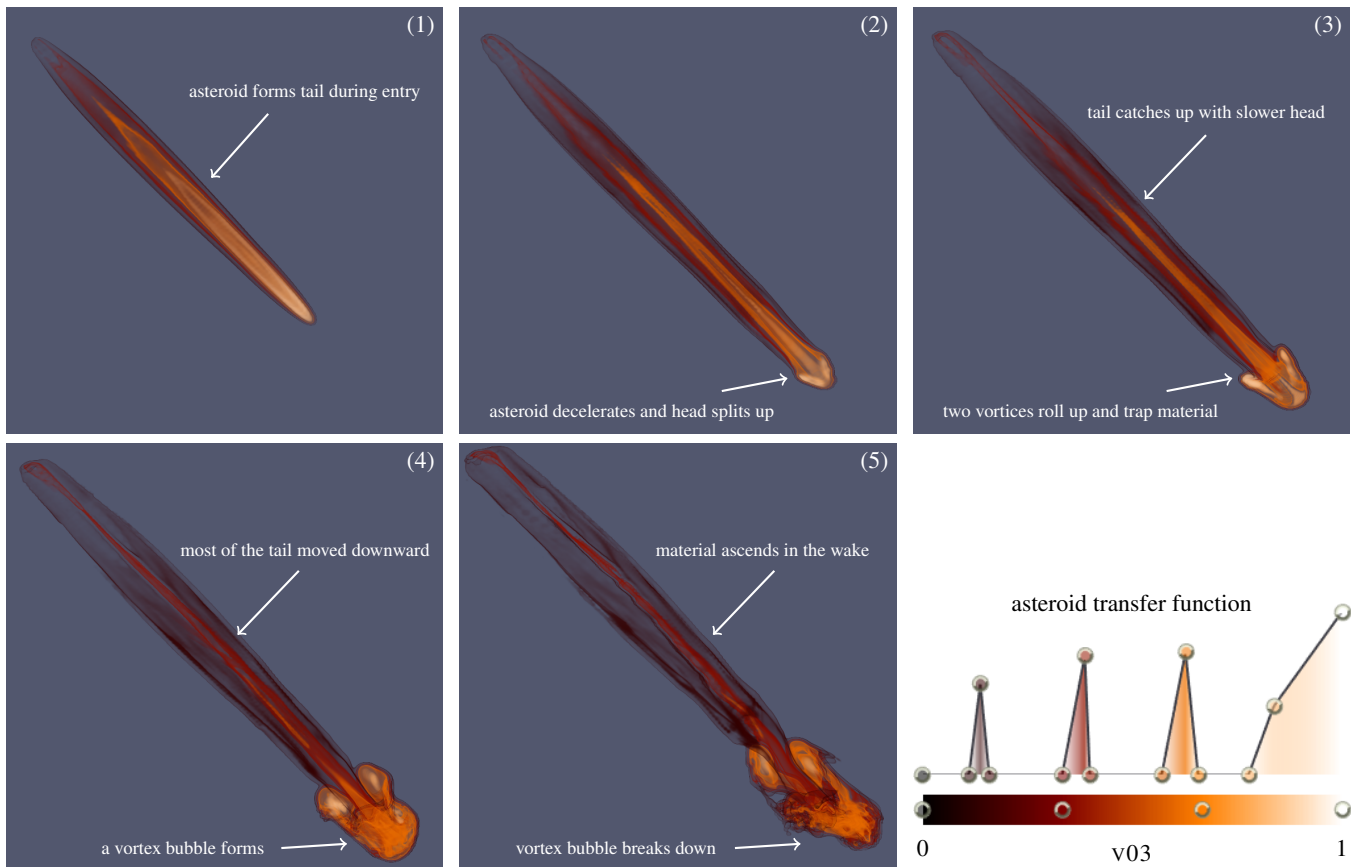
Figure 5: Visualization of the asteroid entry in the YA11 sequence. Here, the asteroid fraction (V03) was rendered with Nvidia IndeX. (1) Upon entry, the asteroid decays and forms a tail. (2) The head decelerates quickly, causing the material in the tail to rush in from behind, which drives the head apart into two pieces. (3) As more tail material moves in, the shear along the entry corridor creates two vortices that trap the asteroid material. (4) Most of the asteroid tail enters a standing vortex bubble. (5) The vortex bubble breaks down and the material slowly ascends in the wake of the asteroid, presumably due to a pressure gradient.
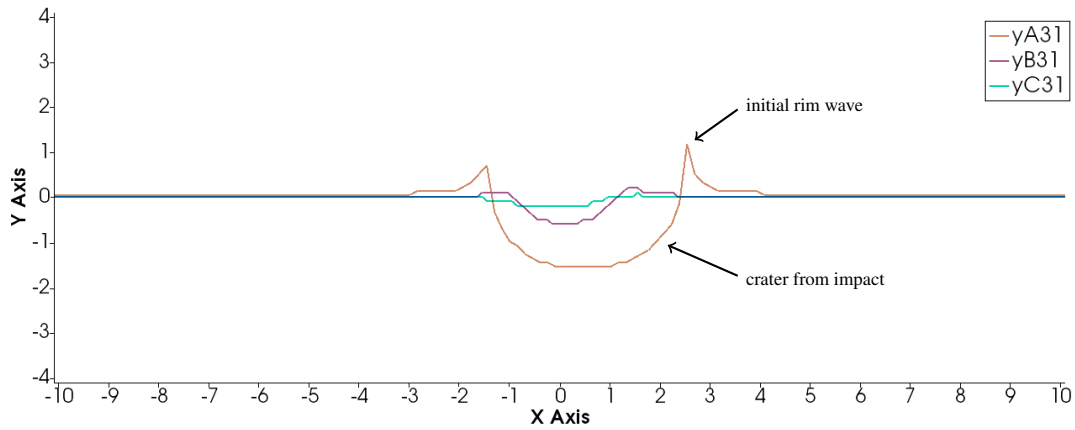
(a) Depending on the height of the airburst (if there was any), the impact creates a crater that is only few meters deep (10 km airburst in YC31), a few hundred meters deep (5 km airburst in YB31) or about 1.5 km deep (no airburst in YA31). Without airburst, the initial rim wave rises about one kilometer above sea level.
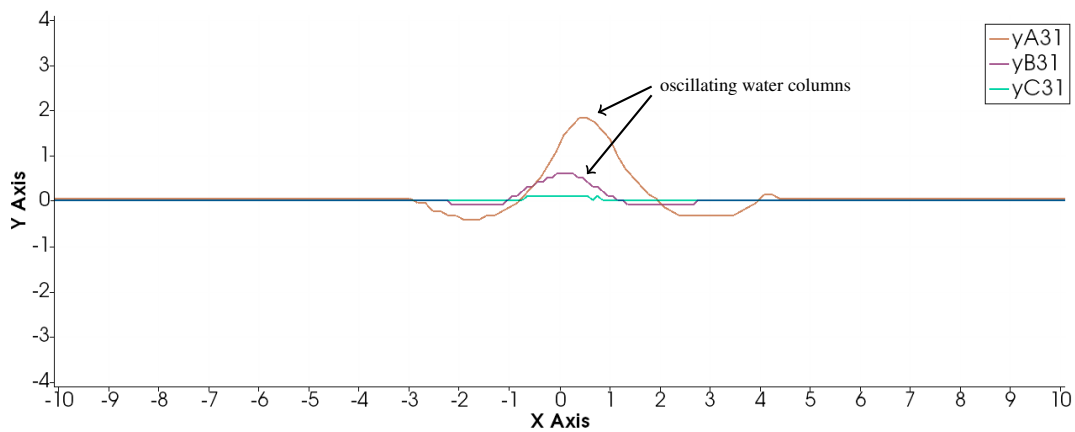

(b) After impact, the water mass starts to vertically oscillate at the impact site, which is dampened over time. Without airburst the crater is so deep that the water rushing back in has enough kinetic energy to raise a water column at the center more than two kilometers high. With airburst, less energy is transferred into the water, resulting in smaller waves.
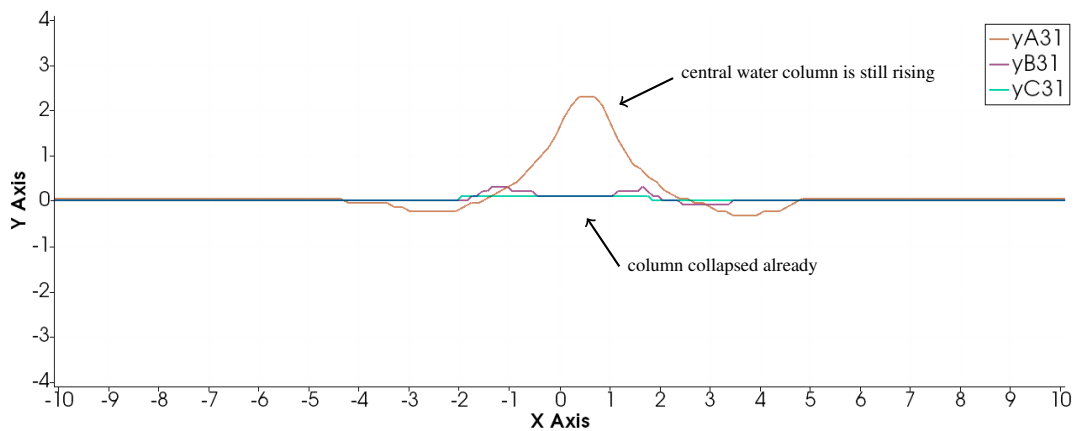
(c) With less kinetic energy from the asteroid, the oscillation frequency is higher. While the central water column of the YA31 asteroid still rises, the columns of the YB31 and YC31 already collapsed, creating smaller secondary waves.

Figure 6: Visualizations of the wave height for different airburst scenarios. The wave height is identified by the largest vertical density gradient.
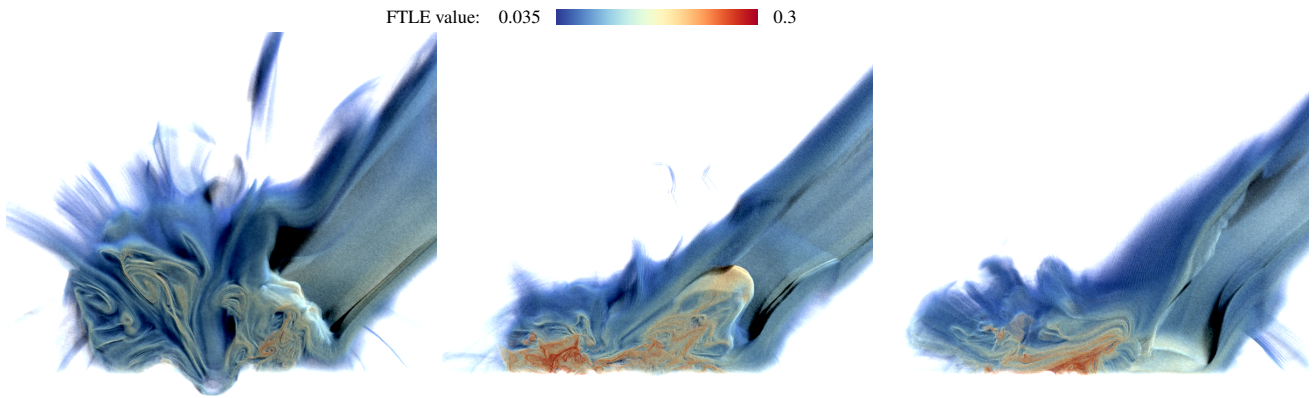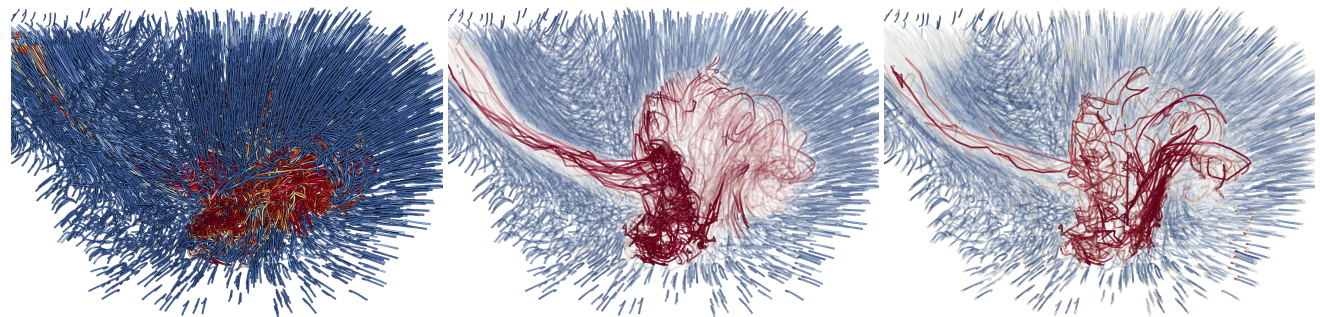
(a) Monte Carlo rendering of the finite-time Lyapunov exponent for the YA31 (left), YB31 (middle) and YC31 (right) series.
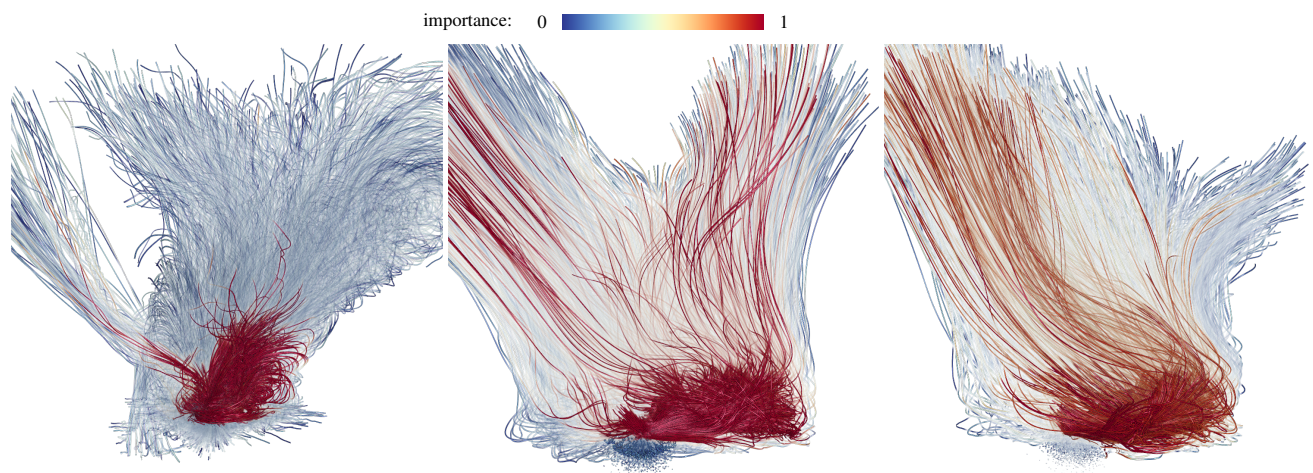

(b) Pathlines for the YA31 (left), YB31 (middle) and YC31 (right) series using opacity optimization to highlight asteroid fraction (V03).


(c) Streaklines in the YA31 data set using opacity optimization to highlight water fraction (middle) and curvature (right), compared to an opaque visualization (left) that exhibits occlusion. Unimportant streaklines (blue) in the context region fade out to clear the view on the important region (red).

Figure 7: These visualization take a Lagrangian approach to the visualization of the fluid flow. The top row displays transport barriers by employing a Monte Carlo rendering technique to show the finite-time Lyapunov exponent [3]. In the second and third row, we visualize integral curve geometry. For this, we use decoupled opacity optimization [5] to highlight selected pathlines (middle) and streaklines (bottom).
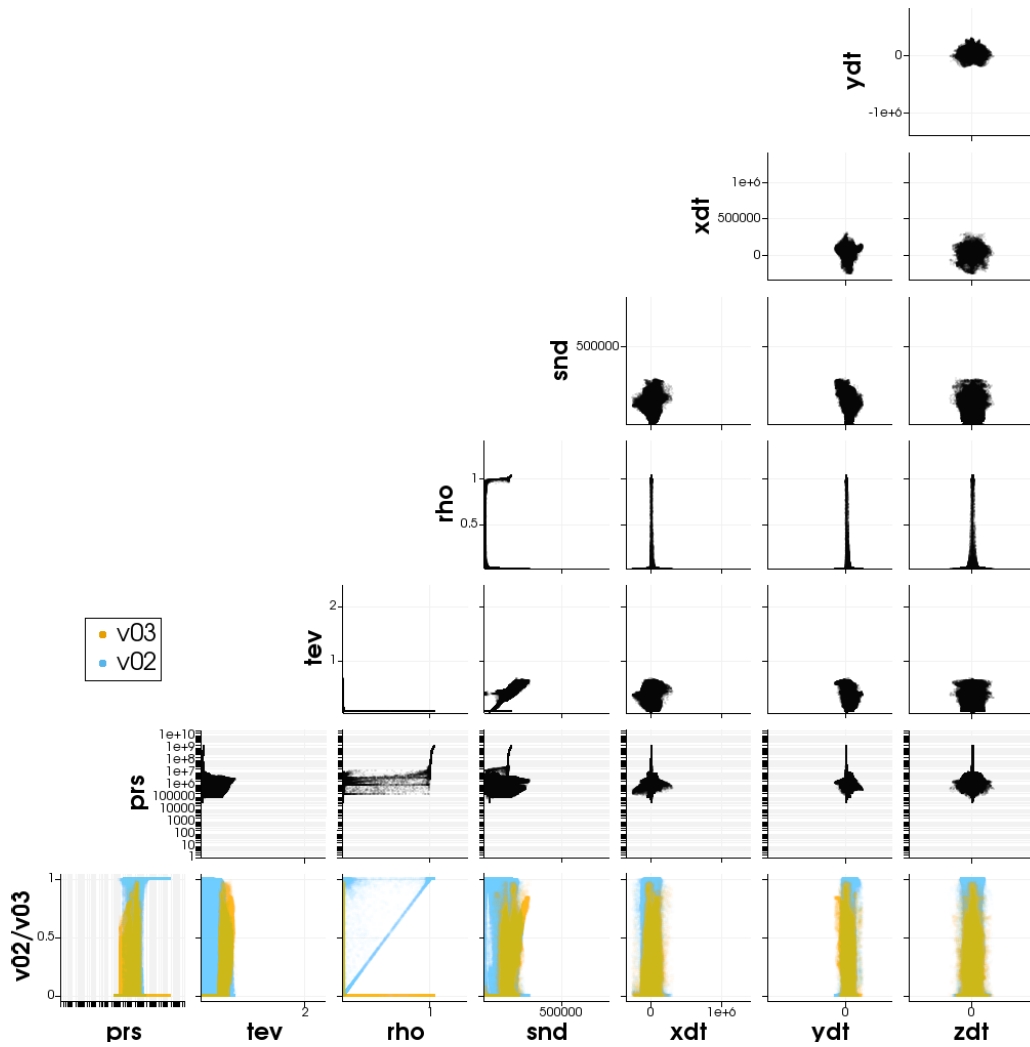
(a) Visualization of selected attributes of the YA31 series in a scatterplot matrix. Each entry in the matrix displays a scatterplot of two attributes, showing correlations and patterns in the data. The bottom row shows plots of the water fraction (V02) and asteroid fraction (V03) together, allowing us to compare the two, showing for instance differences in pressure (PRS), temperature (TEV) and density (RHO).
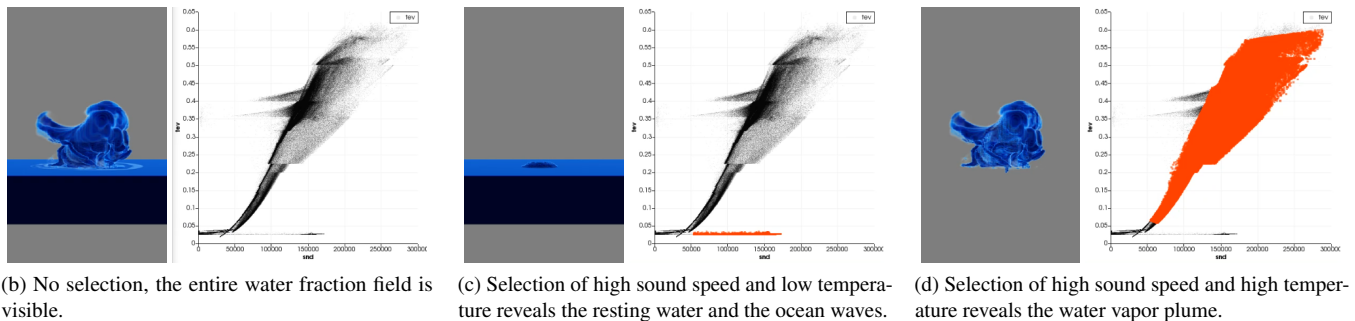

(b) No selection, the entire water fraction field is visible.

(c) Selection of high sound speed and low temperature reveals the resting water and the ocean waves.

(d) Selection of high sound speed and high temperature reveals the water vapor plume.

Figure 8: To allow for an interactive exploration of the multi-variate data, users can view a scatterplot matrix to find correlations and patterns. Here, the user selects a scatterplot in (a) and performs interactive brushing in (b)–(d). Note that the 3D visualization of the water fraction is updated accordingly. Here, shown for the YA31 series (250 m asteroid diameter, no airburst, 45° impact angle).
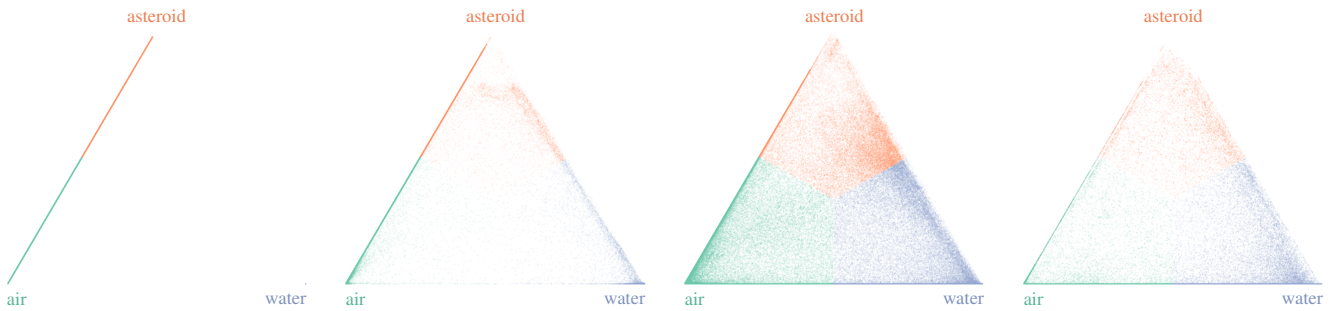
(a) Before impact, asteroid and air are mixed (partial volume effect), and water is largely separate ($t = 1.6$ sec).

(b) Upon impact, water and asteroid start to mix ($t = 2.0$ sec).

(c) As the water vapor plume rises, all three materials mix ($t = 5.2$ sec).

(d) Over time, asteroid material vanishes and all material becomes air, water or a mixture ($t = 27.6$ sec).

Figure 9: Evolution of water fraction (V02), asteroid fraction (V03) and air fraction over time. The images show four time steps, in which each voxel of the data set was splatted into a scatterplot in barycentric coordinates. The animation was computed for the YA31 sequence (250 m asteroid diameter, no airburst, 45° impact angle). The material index (MAT) is color-coded with air (green), water (blue) and asteroid (orange). It can be seen that the material index of a voxel was computed from the fractions, always associating a voxel by the largest fraction therein.
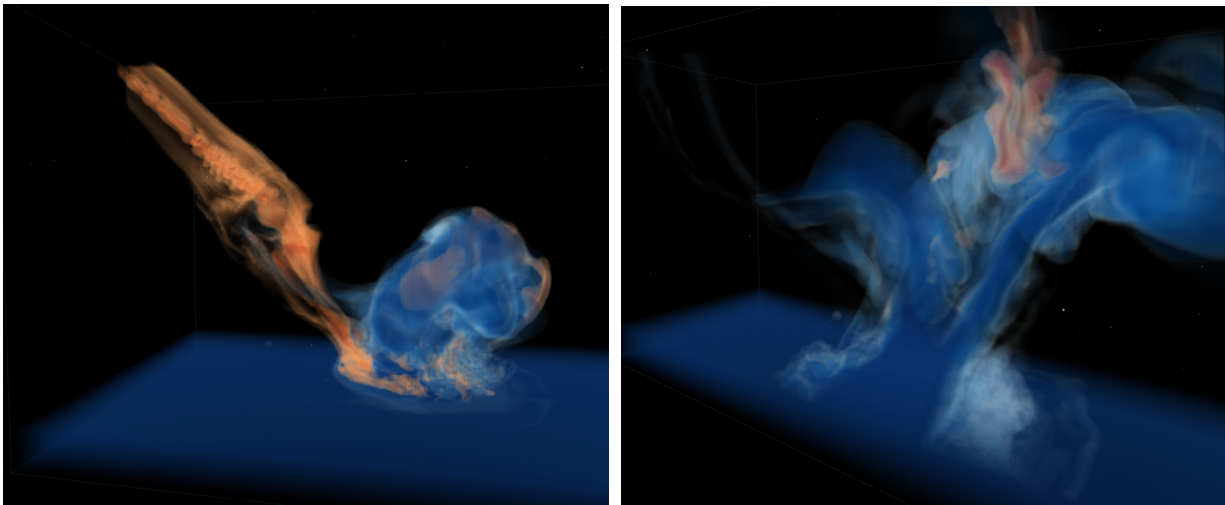
(a) Virtual Reality (VR) demo using an Oculus Rift. The user walks around the scene and adjusts clipping planes.
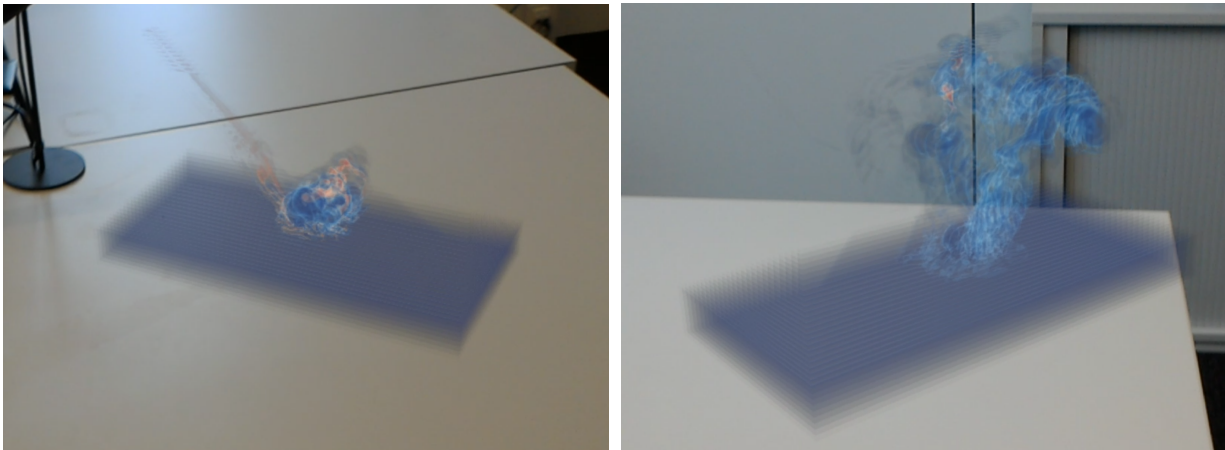
(b) Augmented Reality (AR) demo using a Microsoft HoloLens. The asteroid sequences hovers above a real table.

Figure 10: We employ two different head-mounted devices to explore the interaction capabilities of virtual reality (VR) and augmented reality (AR) in the context of scientific visualization. We found that the wider field of view of the VR device made the 3D exploration more convenient. The user, however, is completely unaware of the surroundings and is bound by cable to a nearby computer. The AR device, on the other hand, embeds the virtual content in the real world, making it possible to interact with other users, which enables a collaborative exploration experience. Since this device operates wireless, users are less restricted in their navigation.